Strong-field photoelectron holography of atoms by bicircular two-color laser pulses

Min Li,[1,2] Wei-Chao Jiang,[1,*] Hui Xie,[2] Siqiang Luo,[2] Yueming Zhou,[2,†] and Peixiang Lu[2,3,‡]

[1]*College of Physics and Energy, Shenzhen University, Shenzhen 518060, China*

[2]*School of Physics and Wuhan National Laboratory for Optoelectronics, Huazhong University of Science and Technology, Wuhan 430074, China*

[3]*Laboratory of Optical Information Technology, Wuhan Institute of Technology, Wuhan 430205, China*

(Received 16 January 2018; published 16 February 2018)

We study photoelectron holography in strong bicircular two-color laser fields by solving the time-dependent Schrödinger equation (TDSE) and a semiclassical rescattering model with implementing interference effect. The holographic patterns observed in the TDSE are well recaptured by the semiclassical rescattering model. Four types of photoelectron holographic interferences between the forward scattered and nonscattered trajectories are predicted by the semiclassical rescattering model in the bicircular two-color laser field. We find that those holographic patterns are spatially separated from each other in the electron momentum distribution. We further show that the dependence of the initial transverse momentum at the tunnel exit on the ionization time for the rescattering electron is recorded by the holographic patterns.

DOI: 10.1103/PhysRevA.97.023415

I. INTRODUCTION

When an atom or a molecule is exposed in a strong laser field, an electron wave packet might be ejected at near the field maximum of the laser field [1]. According to the quantum-orbit theory [2,3], the propagation of the released electron wave packet in the laser field can be approximated by many trajectories. The electron is either freed directly or driven back to the parent ion (known as rescattering), depending on the phase of the laser field when the electron tunnels out from the bound state. The electrons from the rescattering trajectory can have the same final momenta as those from the direct trajectory. The superposition of their contributions in the quantum-mechanical ionization amplitudes leads to the interference in the photoelectron momentum distribution. This kind of interference is very similar to optical holography, thus it is known as strong-field photoelectron holography (SFPH). The SFPH was first observed for strong-field ionization of atoms in a linearly polarized laser field [4,5]. The SFPH can record extensive time-resolved information about both the electron and ion, and it therefore opens a new door to probe ultrafast atomic and molecular dynamics in strong-field physics. Nowadays, the SFPH has been used to characterize the alignment-dependent phase distribution of the tunneling wave packet in molecule [6,7], to extract the phase of the scattering amplitude of atoms and molecules [8], and to probe the molecular dynamics [9,10]. Because the electron-ion rescattering is highly suppressed with increasing the ellipticity of the laser pulse, the SFPH can hardly be observed in a circularly polarized laser field [11].

Almost two decades ago, it was theoretically predicted that the rescattering trajectory can play a considerable role in a bicircular two-color laser field [12,13]. Generally, the bicircular two-color laser field consists of two counterrotating circularly polarized fields with the fundamental frequency and its second harmonic. This special laser wave form is very useful for both high-harmonic generation (HHG) and strong-field ionization (SFI). In the case of HHG, the bicircular two-color laser field has been used to generate high-brightness circularly polarized harmonics in the extreme ultraviolet and soft x-ray regions [14–16], enabling new capabilities for probing magnetic materials and chiral molecules. Recently, it was further demonstrated that the HHG driven by the bicircular two-color laser field has a broad range of applications, such as probing the rotational symmetries of atoms and molecules and their evolution in time [17] and three-dimensional attosecond metrology [18].

In the case of SFI, the bicircular two-color laser pulses have been used to study above-threshold ionization [19,20] and nonsequential double ionization [21–23]. The rescattering trajectory in the bicircular two-color laser field is significantly more complex than that in a linearly polarized laser field [24,25]. Moreover, low-energy features of the electron spectra arising from the electron rescattering were observed, which are separated from the direct ionizations in the final momentum distribution [19]. By changing the laser intensity ratio of the driving laser, the high-energy rescattering electrons were subsequently observed [20]. It is possible that the final momentum of the electron from the rescattering trajectory is the same as that of the electron from the nonscattering trajectory, which can lead to the SFPH in the momentum distribution. The existence of the SFPH in the bicircular two-color laser fields was mentioned by Milošević and Becker [24], but it has not been discussed in detail as far as we know.

In this paper, we study the SFPH in a bicircular two-color laser field by solving the two-dimensional time-dependent

*jiang.wei.chao@szu.edu.cn
†zhouymhust@hust.edu.cn
‡lupeixiang@hust.edu.cn

Schrödinger equation (TDSE) and a semiclassical rescattering model. Four types of photoelectron holographic interferences between the forward-scattered and nonscattered trajectories are predicted by the semiclassical rescattering model in the bicircular two-color laser field, three of which are well resolved in the TDSE simulation. Since the ionization times are mapped to the final two-dimensional momenta for both forward-scattered and nonscattered trajectories, those holographic patterns are separated from each other in the final momentum distributions. In the bicircular two-color laser field, the rescattering electron travels along a two-dimensional trajectory, and the initial transvere momentum of the rescattering electron at the tunnel exit depends sensitively on the ionization time. We show that this dependence has been recorded by the holographic patterns. In addition, we find that the return angle of the rescattering electron also depends sensitively on the ionization time in the bicircular two-color laser field. The wide range of the return angle spanned by the rescattering electron provides an alternative avenue to image the molecular structure and dynamics.

II. METHODS

A. Quantum simulation

To study the SFPH in the bicircular two-color laser fields, we numerically solve the two-dimensional TDSE of a hydrogen atom. The TDSE is expressed as [atomic units (a.u.) are used throughout unless stated otherwise]

$$i\frac{\partial\psi(r,t)}{\partial t} = H(r,t)\psi(r,t), \tag{1}$$

where $\psi(r,t)$ is the wave function and $H(r,t)$ is the Hamiltonian. In length gauge, the Hamiltonian is given by

$$H(r,t) = -\tfrac{1}{2}\nabla^2 + V(r) + \mathbf{r}\cdot\mathbf{E}(t), \tag{2}$$

where r is the distance between the nucleus and the electron. $V(r) = -1/\sqrt{r^2+a}$ is the Coulomb potential. The soft parameter a is set to be 0.635 to match the ionization potential of the hydrogen atom. The electric field of the laser pulse is given by

$$\begin{aligned}\mathbf{E}(t) = {} & E_{1600}f(t)[\cos(\omega t)\hat{x} + \sin(\omega t)\hat{y}] \\ & + E_{800}f(t)[\cos(2\omega t)\hat{x} - \sin(2\omega t)\hat{y}],\end{aligned} \tag{3}$$

where $\hat{x}$ and $\hat{y}$ are the unit vectors along the x and y directions, respectively. E_{1600} and E_{800} are the electric field amplitudes for the 1600-nm and 800-nm pulses, respectively. $f(t) = \sin^2(\pi t/mT)$ is the envelope of the laser pulse with m being the number of the optical cycle and T being the period of the 1600-nm laser field. m is chosen to be 10 in the simulation. The electric field amplitude ratio is chosen to be $E_{800}/E_{1600} = 2$, corresponding to the intensity ratio of $I_{800}/I_{1600} = 4$. It has been shown that the electron-ion rescattering probability is optimized at this intensity ratio [20]. The laser intensity for the fundamental field (1600 nm) is $4\times10^{13}\mathrm{W/cm^2}$ and for the second harmonic (800 nm) is $1.6\times10^{14}\mathrm{W/cm^2}$. Because the photoelectron holography is favored by a longer wavelength [26], we use a long laser wavelength of 1600 nm for the fundamental field. The laser pulse with long wavelength is achievable in the experiment using the optical parametric amplification technology [27]. For this laser field, the ionization mainly occurs in the tunneling ionization regime and the holographic pattern might be easily observed. For the fundamental field with a wavelength of 800 nm, the ionization is dominated by the multiphoton ionization at the intensity ratio of ~4 and the holographic pattern is not well resolved in the final momentum distribution [20].

The initial wave function is obtained by imaginary-time propagation. Then we use the split-operator method to solve the TDSE [28]. At each time step, the whole wave function is separated into the inner and outer regions by a wave-function splitting technique [28]. The wave function in momentum space is calculated by the Fourier transformation of the wave function in the outer region. Then the final momentum distribution is obtained by summing the wave function in momentum space over t_i

$$\frac{\partial P(E,\theta)}{\partial E\partial\theta} = \left|\sum C(\mathbf{p},t_i)\right|^2, \tag{4}$$

where $C(\mathbf{p},t_i)$ is the wave function in the momentum space at each time step t_i, E and θ are the electron energy and the electron emission angle, respectively. In the simulation, the time step is 0.1 a.u. and the grid size of the space is also set to be 0.1 a.u.

B. Semiclassical rescattering model

The rescattering effect in the bicircular two-color laser field has been analyzed in detail by solving the saddle-point equation within the model of the improved strong-field approximation [24,25]. Here we use a simplified semiclassical rescattering model to simulate the interference structures between the nonscattering trajectory and forward-scattering trajectory in the bicircular two-color laser field. This model is based on the classical three-step model and has included the interference effect of the electron trajectories [10,29]. The model has been successfully used to study the holographic structures in a linearly polarized laser field [9,30]. Here we apply it to the analysis of the holographic structure induced by the two-dimensional rescattering trajectories.

For the laser field given by Eq. (3), we neglect the envelope effect. As shown in Fig. 1(a), the electric field $E_s = \sqrt{E_x^2 + E_y^2}$ consists of three segments per cycle, i.e., $-T/6 < t < T/6$, $T/6 < t < T/2$, and $T/2 < t < 5T/6$. Each segment corresponds to a field maximum, thus three electron wave packets can be released within each laser cycle, as shown by w_1, w_2, and w_3 in Fig. 1(a). Due to the threefold rotational symmetry for those three wave packets in the final momentum distribution [24,25], we only consider the rescattering trajectories released from w_1. We restrict the ionization time of the rescattering trajectory within $(0, 0.01T)$, for which the laser field component in the x direction is much larger than that in the y direction. The rescattering trajectory (signal wave) is released at a random laser phase ωt_0 within $(0, 0.01T)$. The velocities of the electron in the x and y directions before the

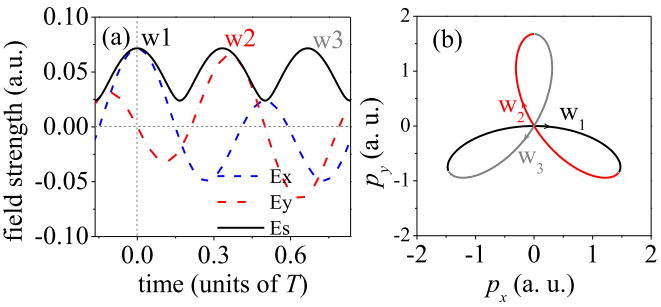

FIG. 1. (a) One cycle of the laser field $E_s = \sqrt{E_x^2 + E_y^2}$ (black curve) is shown. E_x and E_y are the electric fields in the x and y directions, respectively. For better visualization, the two orthogonal components are drawn in parallel. Three electron wave packets (black for w_1, red for w_2, gray for w_3) are launched in each cycle of the laser pulse through the tunneling at near the field maximum. (b) The field-driven photoelectron momenta $\mathbf{p} = -\mathbf{A}(t_0)$ of the three wave packets are shown by the solid curves with different colors. The arrows show the time evolution direction.

rescattering can be written as, respectively,

$$v_x = v_{x0} - \frac{E_0}{\omega}[\sin(\omega t) - \sin(\omega t_0) + \sin(2\omega t) - \sin(2\omega t_0)],$$
$$v_y = v_{y0} + \frac{E_0}{\omega}[\cos(\omega t) - \cos(\omega t_0) - \cos(2\omega t) + \cos(2\omega t_0)], \quad (5)$$

where $E_0 = E_{1600}$. v_{x0} and v_{y0} are the initial momenta in the x and y directions when the electron tunnels, respectively. Because the laser field in the x direction is much larger than that in the y direction for the tunneling phase of $(0, 0.01T)$, we can assume zero initial momentum along the x direction for the rescattering trajectory, i.e., $v_{x0} = 0$. A nonzero initial momentum along the y direction v_{y0} is used to compensate the electron motion induced by the rotating electric field. The rescattering time t_c is determined when the electron is driven back to the core in both x and y directions, i.e., $x(t_c) = 0$ and $y(t_c) = 0$. Due to zero initial momentum along the x direction, we can obtain the rescattering time t_c by numerically solving the equation of motion in the x direction

$$\cos(\omega t_c) - \cos\left(\omega t_0^{\rm sig}\right) + \cos(2\omega t_c)/2 - \cos\left(2\omega t_0^{\rm sig}\right)/2 + \omega\left(t_c - t_0^{\rm sig}\right)\left[\sin\left(\omega t_0^{\rm sig}\right) + \sin\left(2\omega t_0^{\rm sig}\right)\right] = 0, \quad (6)$$

and the initial transverse momentum v_{y0} for the rescattering electron is calculated by,

$$v_{y0} = -E_0/\omega\left[\frac{\sin(\omega t_c) - \sin\left(\omega t_0^{\rm sig}\right)}{\omega\left(t_c - t_0^{\rm sig}\right)} - \frac{\sin(2\omega t_c) - \sin\left(2\omega t_0^{\rm sig}\right)}{2\omega\left(t_c - t_0^{\rm sig}\right)} - \cos\left(\omega t_0^{\rm sig}\right) + \cos\left(2\omega t_0^{\rm sig}\right)\right]. \quad (7)$$

The electron velocities along the x and y directions at the instant of rescattering are given by, respectively,

$$v_{xc} = \frac{E_0}{\omega}\left[\sin(\omega t_c) - \sin\left(\omega t_0^{\rm sig}\right) + \sin(2\omega t_c) - \sin\left(2\omega t_0^{\rm sig}\right)\right],$$
$$v_{yc} = v_{y0} + \frac{E_0}{\omega}\left[\cos(\omega t_c) - \cos\left(\omega t_0^{\rm sig}\right) - \cos(2\omega t_c) + \cos\left(2\omega t_0^{\rm sig}\right)\right]. \quad (8)$$

The return energy E_c and the return angle ϕ_c with respect to the x axis are calculated by

$$E_c = \tfrac{1}{2}\left(v_{xc}^2 + v_{yc}^2\right),$$
$$\phi_c = \tan^{-1}(v_{yc}/v_{xc}). \quad (9)$$

At the instant of rescattering, the electron elastically scatters off the nucleus with a scattering angle θ_c with respect to the impact direction. The scattering angle θ_c is within $[-90^\circ, 90^\circ]$ for the forward scattering. Thus the final momentum of the rescattering electron is given by

$$p_x = \sqrt{2E_c}\cos(\phi_c - \theta_c) + \frac{E_0}{\omega}[\sin(\omega t_c) + \sin(2\omega t_c)],$$
$$p_y = \sqrt{2E_c}\sin(\phi_c - \theta_c) - \frac{E_0}{\omega}[\cos(\omega t_c) - \cos(2\omega t_c)]. \quad (10)$$

We mainly discuss the interference between the rescattering and nonscattering trajectories. Those electrons tunnel at different times, travel along different paths, and obtain the same final momenta. Given the final momenta, we can directly calculate the ionization time and the initial transverse momentum for the nonscattering electron (reference wave)

$$\mathbf{p} = \mathbf{v}\left(t_0^{\rm ref}\right) - \mathbf{A}\left(t_0^{\rm ref}\right), \quad (11)$$

where $t_0^{\rm ref}$ is the ionization time of the nonscattering electron, $\mathbf{A}(t)$ is the vector potential of the laser field at the time t, and $\mathbf{v}(t)$ is the initial momentum transverse to the instantaneous laser field when the electron tunnels. The phase of each trajectory is given by the classical action along the path, i.e., $S = \int_{t_0}^{\infty}(\frac{\mathbf{v}^2(t)}{2} + I_p)dt$. Therefore, the phase difference between the forward-scattering and nonscattering trajectories is

$$\Delta S = \frac{1}{2}\int_{t_0^{\rm sig}}^{t_c}\left(v_x^2 + v_y^2\right)dt - \frac{1}{2}\int_{t_0^{\rm ref}}^{t_c}\left(v_x^2 + v_y^2\right)dt - I_p\left(t_0^{\rm sig} - t_0^{\rm ref}\right). \quad (12)$$

The interference patterns are determined by this phase difference, i.e., $W = \cos^2(\Delta S/2)$. In this model, we sample the electron ensemble with the Monte Carlo method.

Compared to the quantum-orbit theory [24,25], the semiclassical rescattering model need not solve the saddle-point equation. With neglecting the initial momentum along the x direction, the two-dimensional rescattering problem of an electron in a bicircular two-color laser field is much simplified, i.e., we need only numerically solve Eq. (6) to obtain the rescattering time t_c for a given ionization time t_0, and all other physical quantities can be analytically obtained.

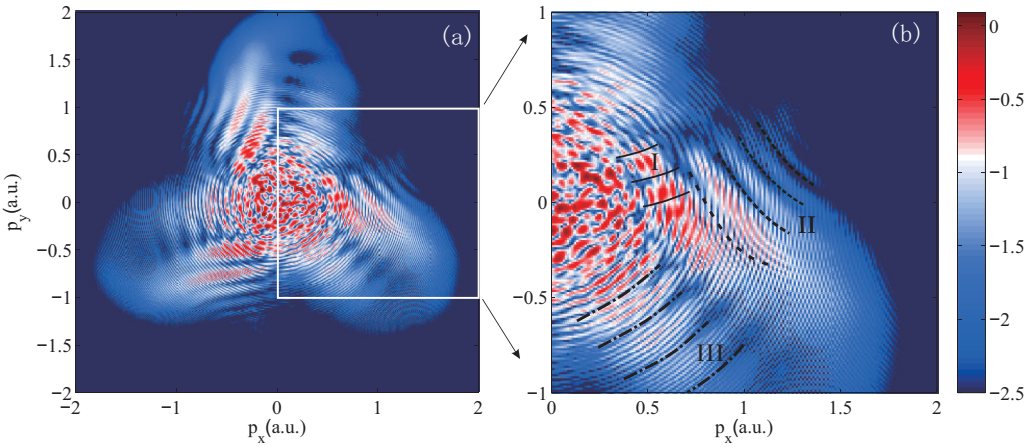

FIG. 2. (a) Logarithm of the differential ionization rate of H atoms presented in false colors in the electron momentum plane for ionization by a bicircular two-color laser field by solving the TDSE. The intensity for 1600-nm laser pulse is $4 \times 10^{13}\mathrm{W/cm^2}$ and for 800-nm laser pulse is $1.6 \times 10^{14}\,\mathrm{W/cm^2}$. Panel (b) shows the enlarged momentum distribution inside the white frame of (a) to highlight different interference patterns marked as I, II, and III. The solid, dashed, and dot-dashed lines show the minima of the interference patterns I, II, and III, respectively.

III. RESULTS AND DISCUSSIONS

Since the rescattering trajectory is more complex than the nonscattering trajectory in the bicircular two-color laser field, we first estimate the final momentum distribution of the nonscattering electron. With neglecting the Coulomb potential and the initial momentum at the instant of tunneling, the final momentum of a nonscattering electron can be estimated by the field-driven momentum $\mathbf{p} = -\mathbf{A}(t_0)$. In Fig. 1(b), we show the field-driven momenta for the three wave packets of Fig. 1(a) (black for w_1, red for w_2, gray for w_3). One can see that the distribution of the field-driven momentum shows a three-lobe structure. Each wave packet contributes to an arc of the three-lobe structure.

A. Interference patterns in TDSE

To study the photoelectron interference effect, we show in Fig. 2(a) the photoelectron momentum distributions by solving the TDSE. As expected, the photoelectron momentum distribution by solving the TDSE shows a threefold rotational symmetry [24]. Three arcs can be clearly seen in the photoelectron momentum distribution, which correspond to the three nonscattering wave packets released within one laser cycle by comparison to Fig. 1(b). One can see that those three nonscattering wave packets are separated from each other in the momentum distributions except for the low-energy photoelectron with $p_r = \sqrt{p_x^2 + p_y^2} < 0.4$ a.u.

More importantly, the TDSE result reveals many interesting interference patterns. First, the spectrum displays ring-like interference patterns centered around zero momentum, which come from the intercycle interference of the electron wave packets [31]. Besides those ring-like patterns, there are three other prominent interference structures. We show in Fig. 2(b) an enlarged view for the momentum distribution inside the white frame of Fig. 2(a), where the three obvious interference patterns are marked as I, II, and III. Those three interference patterns differ from each other by the slopes of their interference fringes. One can see that the interference patterns I and II are very similar to the spider-leg structure in a linearly polarized laser field [4]. In contrast to the spider-leg structure in the linearly polarized laser field, the patterns I and II are not symmetric with respect to $p_y = 0$. The interference pattern I shows many tilted fringes with positive slope while the interference pattern II reveals many tilted fringes with negative slope. The third interference pattern III also shows many tilted fringes with positive slope, which are nearly perpendicular to the fringes of the interference pattern II. Moreover, those three kinds of interference patterns are distributed in different regions of the final momentum plane. Comparing Fig. 2(b) to Fig. 1(b), one can find that the interference patterns I and II appear in the region of the electron momentum plane corresponding to the nonscattering electron wave packet w_1 [black curve in Fig. 1(b)] and the interference pattern III appears in the region of the electron momentum plane corresponding to the nonscattering electron wave packet w_2 [red curve in Fig. 1(b)]. Those interference patterns are not well resolved in TDSE using the laser pulse with a shorter wavelength of 800 nm for the fundamental field [32].

B. Holography by semiclassical rescattering model

To shed light on the origins of the interference patterns in TDSE, we resort to the semiclassical rescattering model. Before showing the interference patterns, let us study the rescattering trajectory in the bicircular two-color laser field. In Figs. 3(a) and 3(b), we show the return energy and the return angle of the rescattering trajectories with respect to the ionization (and rescattering) time. The return energy and the return angle are defined in Eq. (9). For comparison, the results in a linearly polarized laser field are also shown (dashed curves). In a linearly polarized laser field, one can see that the curve of the return energy with respect to the ionization time (or the rescattering time) shows a single-peak structure. The electron freed at $\sim 0.047T$ ($\sim 17^\circ$) obtains the maximum return energy of $3.17U_p$, where U_p is the ponderomotive energy. In contrast, the curve of the return energy with respect to the ionization time (or the rescattering time) reveals a double-peak structure in the bicircular two-color laser field [33], as shown

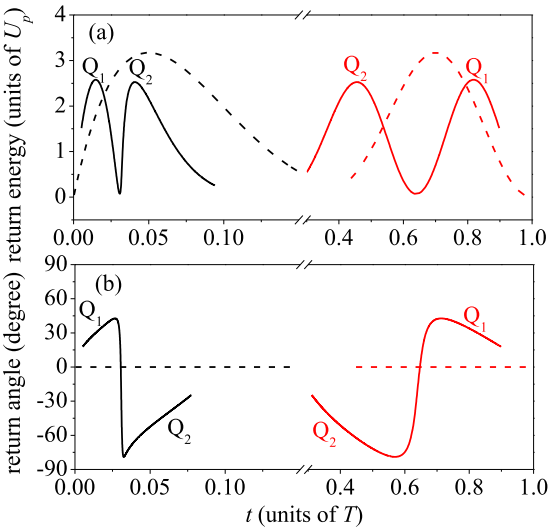

FIG. 3. The return energy and return angle of the rescattering electron with respect to the ionization time (black) and the rescattering time (red). The return energy and the return angle are defined in Eq. (9). The dashed curves show the results in a linearly polarized laser field.

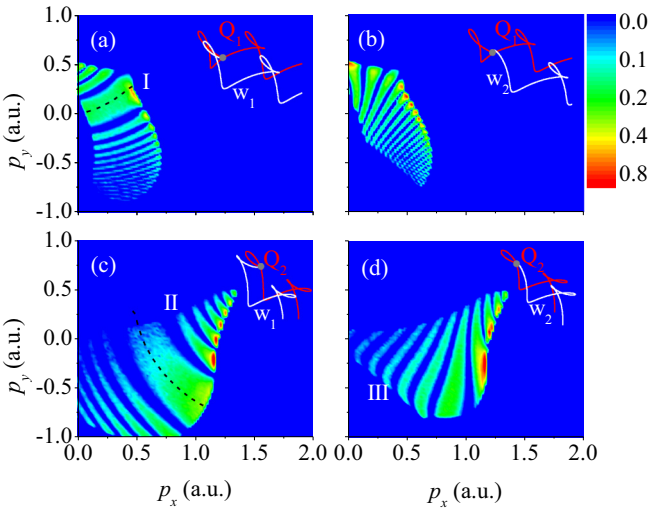

FIG. 4. (a) The simulated holographic structures from the interferences of rescattering trajectory Q_1 with nonscattering trajectory w_1, (b) rescattering trajectory Q_1 with nonscattering trajectory w_2, (c) rescattering trajectory Q_2 with nonscattering trajectory w_1, (d) and rescattering trajectory Q_2 with nonscattering trajectory w_2 are shown using the classical recollision model. Here the ionization rate of the trajectory is not included. The black dashed lines in (a) and (c) show the central maxima of the corresponding interference fringes. (a) I, (c) II, and (d) III are used to show the same interference patterns as those in Fig. 2(b). Inset: Typical trajectories of the corresponding interference patterns. The red curves are the forward scattering trajectories and the white curves are the nonscattering trajectories. A scattering angle of 10° at the instant of rescattering is assumed for the forward rescattering trajectory. The gray dots show the positions of the parent ions.

by the solid curves. Those two peaks are marked as Q_1 and Q_2 in Fig. 3(a), which are separated by the ionization time of $\sim 0.03T$ (or the rescattering time of $\sim 0.65T$). Near zero return energy is obtained by the electron released at $\sim 0.03T$. The electron released before $\sim 0.03T$ (Q_1 trajectory) returns to the nucleus later while the electron released after $\sim 0.03T$ (Q_2 trajectory) returns to the nucleus earlier. At the ionization times of $\sim 0.014T$ and $\sim 0.041T$, the electron obtains the maximum return energy of $\sim 2.58U_p$, where the U_p of the bicircular two-color field is simply the sum of the U_p of each field. This cutoff energy agrees well with the prediction in Ref. [13].

For the return angle, as shown by the dashed lines in Fig. 3(b), the electron returns to the nucleus with zero degree in a linearly polarized laser field. In the bicircular two-color laser field, the rescattering electron travels along a two-dimensional trajectory with a nonzero return angle. The return angle of the trajectory Q_1 changes from $\sim 5°$ to $\sim 45°$, while the return angle for the trajectory Q_2 changes from $\sim -90°$ to $\sim -20°$, as shown by the solid curves in Fig. 3(b).

Those rescattering trajectories of Q_1 and Q_2 can interfere with the nonscattering trajectories w_1 and w_2 when their final momenta are the same. Therefore, there might be four kinds of interferences between the forward scattering and nonscattering trajectories, i.e., the interference of rescattering trajectory Q_1 with nonscattering trajectory w_1, rescattering trajectory Q_1 with nonscattering trajectory w_2, rescattering trajectory Q_2 with nonscattering trajectory w_1, and rescattering trajectory Q_2 with nonscattering trajectory w_2. In Fig. 4, we show those four kinds of interferences using the semiclassical rescattering model. The insets show typical trajectories contributing to the corresponding interference patterns.

The interference of Q_1 with w_1 [Fig. 4(a)] reveals many fringes with positive slope, and the fringe space is similar to the interference pattern I in Fig. 2(b). Both of them mainly appear in the electron momentum plane with p_x ranging from 0.1 to 0.5 a.u. and p_y ranging from -0.3 to 0.3 a.u.. Thus, the interference pattern I in Fig. 2(b) results from the interference of Q_1 with w_1. The interference fringes of Q_2 with w_1 [Fig. 4(c)] reveal negative slopes, which agree qualitatively with the interference pattern II of Fig. 2(b). Specifically, the fringes are nearly the same for those two patterns when p_x changes from 1 to 1.5 a.u.. Therefore, the interference pattern II in Fig. 2(b) results from the interference of Q_2 with w_1. The interference of Q_1 with w_2 [Fig. 4(b)] shows many stripes with smaller spacing, while the interference of Q_2 with w_2 [Fig. 4(d)] reveals stripes with larger spacing. The interference of Q_2 with w_2 agrees with the interference pattern III of Fig. 2(b) because their fringe spacings are very similar. And the slopes of the fringes at $p_x = 0.5$ a.u. are also similar for the interference structure of Fig. 4(d) and the interference pattern III of Fig. 2(b). Therefore, the pattern III in Fig. 2(b) originates from the interference of Q_2 with w_2. Using the semiclassical rescattering model, we provide a physical interpretation of different kinds of interferences in the TDSE result of Fig. 2(b).

To further estimate the contributions of different holographic structures to the momentum distribution, we can study the most probable trajectories released at different ionization times for both nonscattering and rescattering electrons. Here the most probable trajectory indicates the (nonscattering or rescattering) trajectory with the largest ionization probability for a given ionization time. For the nonscattering electron,

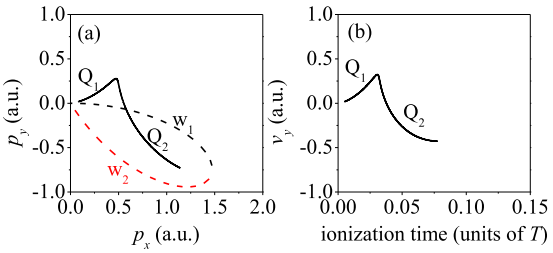

FIG. 5. (a) The solid curves show the final momenta of the rescattering trajectories Q_1 and Q_2 with zero scattering angle at the instant of rescattering. The dashed curves show the final momenta of the nonscattering trajectories w_1 and w_2 with $\mathbf{p} = -\mathbf{A}(t_0)$. (b) The initial transverse momentum with respect to the ionization time for the rescattering trajectories Q_1 and Q_2.

the most probable trajectory corresponds to the electron released with zero initial momentum according to the tunneling theory [34]. For the forward scattering electron, the initial momentum is determined by the ionization time according to Eq. (6), and thus the most probable trajectory corresponds to the electron with zero scattering angle due to the divergent scattering cross section of the Coulomb potential [35]. In Fig. 5(a), we show the final momenta of the most probable trajectories for the rescattering electrons Q_1 and Q_2 (solid lines) and for the nonscattering electrons w_1 and w_2 (dashed lines). The momentum distribution of the rescattering and nonscattering electron wave packets will be centered by the momenta of the corresponding most probable trajectory, and the holographic pattern appears only when both signals from the rescattering and nonscattering wave packets are large. From Fig. 5(a), one can predict that the interference of Q_1 with w_1 will be obvious when p_x is within $[0.1, 0.5]$ a.u. and p_y is within $[-0.1, 0.3]$ a.u. due to the large overlap of the rescattering and nonscattering wave packets. This agrees well with the TDSE result in Fig. 2(b). Because the final momentum of the most probable nonscattering trajectory w_1 locates in the upper right side of Q_2 in Fig. 5(a), the interference structure of Q_2 with w_1 will mainly appear in the upper right side of the solid line of Q_2. Similarly, the interference structure of Q_2 with w_2 will mainly appear in the lower left side of the solid line Q_2 of Fig. 5(a). Those features are also in good agreement with the interference patterns II and III in Fig. 2(b). Due to the large difference between the final momenta of the most probable trajectories Q_1 and w_2, as shown in Fig. 5(a), the interference of Q_1 with w_2 will be suppressed. As shown in Fig. 2(b), this kind of interference is indeed not resolved in TDSE.

Because the momenta of the most probable trajectories for the rescattering and nonscattering electrons are distributed in different regions of the momentum plane, the holographic structures are also spatially separated from each other, as shown in Fig. 2(b). The separation of different types of interferences in the final momentum distribution makes it easier to retrieve the information of the electronic dynamics from the interference pattern. If multiple interference patterns are mixed with each other, a minimum of one type of interference might be overlapped by a maximum of another type, which will reduce the precision of the phase reconstruction [36,37].

There are still some differences between the simulated interference patterns from the TDSE [Fig. 2(b)] and semiclassical rescattering model [Figs. 4(a), 4(c) and 4(d)] by a careful comparison. Two reasons might be responsible for the differences. One is the effect of the long-range Coulomb potential on the electron trajectory, which is neglected in the semiclassical rescattering model. The other one is that the nonadiabatic effect is not considered in the semiclassical rescattering model [38].

C. Imprint of the initial transverse momentum in the holographic patterns

In the bicircular two-color laser field, the rescattering electron travels along a two-dimensional trajectory in the laser polarization plane. As a result, only the electron with a specific initial transverse momentum at the tunnel exit can be driven back to the parent ion. Within the semiclassical rescattering model, the initial transverse momentum of the rescattering electron should satisfy Eq. (7) for a given ionization time. Thus the value of the initial transverse momentum at the tunnel exit depends on the ionization time. In Fig. 5(b), we show the initial transverse momentum of the rescattering trajectory with respect to the ionization time in the bicircular two-color laser field. One sees that the initial transverse momentum v_{y0} for the rescattering trajectory Q_1 [the ionization time of $(0, 0.03T)$] increases with the increase of the ionization time, while decreases with the increase of the ionization time for the rescattering trajectory Q_2 [the ionization time of $(0.03T, 0.1T)$].

Because the vector potential of the laser field along the y direction is negligible at the ionization time of $(0, 0.1T)$, the final momenta of the most probable rescattering trajectories (zero scattering angle) are $p_x \approx \frac{E_0}{\omega}[\sin(\omega t_0) + \sin(2\omega t_0)]$ and $p_y \approx v_{y0}$, according to Eq. (10). As a result, the dependence of the initial transverse momentum v_{y0} on the ionization time t_0 is mapped to the final two-dimensional momenta (p_y with respect to p_x) for the most probable rescattering trajectories. As shown by the solid curves in Fig. 5(a), we see that p_y increases when p_x increases from 0 to 0.55 a.u., while p_y decreases when p_x increases from 0.55 to 1.2 a.u. for the most probable rescattering trajectories. More importantly, the final momenta of the most probable rescattering trajectories correspond to the central maxima of the holographic patterns in Figs. 4(a) and 4(c) because the phase difference between the rescattering and nonscattering trajectories is zero for zero scattering angle, according to Eq. (12). As shown in Figs. 4(a) and 4(c), the central maxima of the interference fringes indeed show the same structure as that in Fig. 5(b), i.e., the interference structure of the rescattering trajectory Q_1 [Fig. 4(a)] reveals fringes with positive slope while the interference structure of the rescattering trajectory Q_2 [Fig. 4(c)] reveals fringes with negative slope. The holographic patterns have recorded the dependence of the initial transverse momentum at the tunnel exit on the ionization time for the rescattering electron in the bicircular two-color laser field.

IV. CONCLUSION

In conclusion, we systematically study the photoelectron holography in strong bicircular two-color laser fields using numerical solutions of the TDSE and the semiclassical rescattering model. We predict four types of photoelectron holographic

interferences between the forward scattered and nonscattered trajectories in the bicircular two-color laser field using the semiclassical rescattering model. In the TDSE simulation, three types of the interference patterns can be well resolved. We find that those holographic patterns are spatially separated from each other in the final momentum distribution, which is significant for retrieving the information about the electronic dynamics from those holographic patterns [6–8]. We find that only the electron with a specific initial transverse momentum at the tunnel exit can be driven back to the parent ion in the bicircular two-color laser field, and the value of the initial transverse momentum depends sensitively on the ionization time. It is further shown that the dependence of the initial transverse momentum on the ionization time for the rescattering electron has been recorded by the holographic patterns.

It is well known that the rescattering electron has been widely used to image the molecular structure. Unlike the case in a linearly polarized laser field, the rescattering electrons travel along two-dimensional trajectories in the laser polarization plane in a bicircular two-color laser field. The return angle is altered with respect to the ionization time, as shown in Fig. 3(b). This makes the photoelectron holographic structure valuable for probing electronic dynamics in molecules. The molecular structure might be more easily imaged because of the wide range of the return angles. When the bicircular two-color laser field is used to ionize a molecule, the rotational symmetry for the photoelectron momentum distribution and the holographic structure might be broken. Thus the photoelectron holographic structure might be applied as a sensitive probe of the electronic structure and symmetry-breaking process of molecules [17].

ACKNOWLEDGMENTS

This work was supported by the National Natural Science Foundation of China under Grants No. 61405064, No. 11722432, No. 11747013, No. 11674116, and No. 11234004 and the Fundamental Research Funds for the Central University, HUST: 2016YXMS012.

[1] L. V. Keldysh, Sov. Phys. JETP **20**, 1307 (1965).
[2] P. Salières, B. Carré, L. Le Déroff, F. Grasbon, G. G. Paulus, H. Walther, R. Kopold, W. Becker, D. B. Milošević, A. Sanpera, and M. Lewenstein, Science **292**, 902 (2001).
[3] W. Becker, F. Grabon, R. Kopold, D. B. Milošević, G. G. Paulus, and H. Walther, Adv. At. Mol. Opt. Phys. **48**, 35 (2002).
[4] Y. Huismans *et al.*, Science **331**, 61 (2011); Phys. Rev. Lett. **109**, 013002 (2012).
[5] D. D. Hickstein, P. Ranitovic, S. Witte, X.-M. Tong, Y. Huismans, P. Arpin, X. Zhou, K. E. Keister, C. W. Hogle, B. Zhang, C. Ding, P. Johnsson, N. Toshima, M. J. J. Vrakking, M. M. Murnane, and H. C. Kapteyn, Phys. Rev. Lett. **109**, 073004 (2012).
[6] M. Meckel, A. Staudte, S. Patchkovskii, D. M. Villeneuve, P. B. Corkum, R. Dörner, and M. Spanner, Nat. Phys. **10**, 594 (2014).
[7] M.-M. Liu, M. Li, C. Wu, Q. Gong, A. Staudte, and Y. Liu, Phys. Rev. Lett. **116**, 163004 (2016).
[8] Y. Zhou, O. I. Tolstikhin, and T. Morishita, Phys. Rev. Lett. **116**, 173001 (2016); M. He, Y. Li, Y. Zhou, M. Li, and P. Lu, Phys. Rev. A **93**, 033406 (2016); M. He, Y. Zhou, Y. Li, M. Li, and P. Lu, Opt. Quant. Eletron. **49**, 232 (2017).
[9] X.-B. Bian, Y. Huismans, O. Smirnova, K.-J. Yuan, M. J. J. Vrakking, and A. D. Bandrauk, Phys. Rev. A **84**, 043420 (2011).
[10] M. Haertelt, X.-B. Bian, M. Spanner, A. Staudte, and P. B. Corkum, Phys. Rev. Lett. **116**, 133001 (2016).
[11] W. Yang, Z. Sheng, X. Feng, M. Wu, Z. Chen, and X. Song, Opt. Express **22**, 2519 (2014).
[12] S. Long, W. Becker, and J. K. McIver, Phys. Rev. A **52**, 2262 (1995).
[13] D. B. Milošević, W. Becker, and R. Kopold, Phys. Rev. A **61**, 063403 (2000).
[14] A. Fleischer, O. Kfir, T. Diskin, P. Sidorenko, and O. Cohen, Nat. Photonics **8**, 543 (2014).
[15] O. Kfir *et al.*, Nat. Photonics **9**, 99 (2015).
[16] T. Fan *et al.*, Proc. Natl. Acad. Sci. USA **112**, 14206 (2015); C. Zhai, X. Zhang, X. Zhu, L. He, Y. Zhang, B. Wang, Q. Zhang, P. Lan, and P. Lu, Opt. Express **26**, 2775 (2018).
[17] D. Baykusheva, M. S. Ahsan, N. Lin, and H. J. Wörner, Phys. Rev. Lett. **116**, 123001 (2016).
[18] C. Chen, Z. Tao, C. Hernández-García, P. Matyba, A. Carr, R. Knut, O. Kfir, D. Zusin, C. Gentry, P. Grychtol, O. Cohen, L. Plaja, A. Becker, A. Jaron-Becker, H. Kapteyn, and M. Murnane, Sci. Adv. **2**, e1501333 (2016).
[19] C. A. Mancuso, D. D. Hickstein, P. Grychtol, R. Knut, O. Kfir, X.-M. Tong, F. Dollar, D. Zusin, M. Gopalakrishnan, C. Gentry, E. Turgut, J. L. Ellis, M.-C. Chen, A. Fleischer, O. Cohen, H. C. Kapteyn, and M. M. Murnane, Phys. Rev. A **91**, 031402(R) (2015).
[20] C. A. Mancuso, D. D. Hickstein, K. M. Dorney, J. L. Ellis, E. Hasović, R. Knut, P. Grychtol, C. Gentry, M. Gopalakrishnan, D. Zusin, F. J. Dollar, X.-M. Tong, D. B. Milošević, W. Becker, H. C. Kapteyn, and M. M. Murnane, Phys. Rev. A **93**, 053406 (2016).
[21] C. A. Mancuso, K. M. Dorney, D. D. Hickstein, J. L. Chaloupka, J. L. Ellis, F. J. Dollar, R. Knut, P. Grychtol, D. Zusin, C. Gentry, M. Gopalakrishnan, H. C. Kapteyn, and M. M. Murnane, Phys. Rev. Lett. **117**, 133201 (2016).
[22] S. Eckart, M. Richter, M. Kunitski, A. Hartung, J. Rist, K. Henrichs, N. Schlott, H. Kang, T. Bauer, H. Sann, L. Ph. H. Schmidt, M. Schöffler, T. Jahnke, and R. Dörner, Phys. Rev. Lett. **117**, 133202 (2016).
[23] J. L. Chaloupka and D. D. Hickstein, Phys. Rev. Lett. **116**, 143005 (2016); Y. Zhou, M. Li, Y. Li, A. Tong, Q. Li, and P. Lu, Opt. Express **25**, 8450 (2017).
[24] D. B. Milošević and W. Becker, Phys. Rev. A **93**, 063418 (2016).
[25] E. Hasović, W. Becker, and D. B. Milošević, Opt. Express **24**, 6413 (2016).
[26] T. Marchenko, Y. Huismans, K. J. Schafer, and M. J. J. Vrakking, Phys. Rev. A **84**, 053427 (2011).
[27] S. Rezvani, Z. Hong, X. Pang, S. Wu, Q. Zhang, and P. Lu, Opt. Lett. **42**, 3367 (2017); Z. Hong, Q. Zhang, S. Rezvani, P. Lan, and P. Lu, Opt. Laser Technol. **98**, 169 (2018).
[28] Y. Li, M. Li, Y. Zhou, X. Ma, H. Xie, P. Lan, and P. Lu, Opt. Express **25**, 11233 (2017); B. Wang, L. He, F. Wang, H. Yuan, X. Zhu, P. Lan, and P. Lu, Phys. Rev. A **97**, 013417 (2018);

J. Tan, Y. Zhou, M. He, Y. Chen, M. Li, and P. Lu, Opt. Quantum Electron. **50**, 57 (2018).
[29] G. G. Paulus, W. Becker, W. Nicklich, and H. Walther, J. Phys. B **27**, L703 (1994).
[30] H. Xie, M. Li, Y. Li, Y. Zhou, and P. Lu, Opt. Express **24**, 27726 (2016).
[31] M. Li, J.-W. Geng, Hong Liu, Y. Deng, C. Wu, L.-Y. Peng, Q. Gong, and Y. Liu, Phys. Rev. Lett. **112**, 113002 (2014).
[32] V.-H. Hoang, V.-H. Le, C. D. Lin, and A.-T. Le, Phys. Rev. A **95**, 031402(R) (2017).
[33] X. Zhang, L. Li, X. Zhu, X. Liu, Q. Zhang, P. Lan, and P. Lu, Phys. Rev. A **94**, 053408 (2016).
[34] N. B. Delone and V. P. Krainov, J. Opt. Soc. Am. B **8**, 1207 (1991).
[35] M. Möller, F. Meyer, A. M. Sayler, G. G. Paulus, M. F. Kling, B. E. Schmidt, W. Becker, and D. B. Milošević, Phys. Rev. A **90**, 023412 (2014).
[36] D. G. Arbó, K. L. Ishikawa, K. Schiessl, E. Persson, and J. Burgdörfer, Phys. Rev. A **82**, 043426 (2010).
[37] X. Xie, Phys. Rev. Lett. **114**, 173003 (2015).
[38] M. Li, J. W. Geng, M. Han, M.-M. Liu, L. Y. Peng, Q. Gong, and Y. Liu, Phys. Rev. A **93**, 013402 (2016); **95**, 053425 (2017).